

Beam dynamics studies with the heavy-ion linear induction accelerator MBE-4

W. M. Fawley,^{a)} T. Garvey,^{b)} S. Eylon, E. Henestroza, A. Faltens, T. J. Fessenden, K. Hahn, and L. Smith

Lawrence Berkeley National Laboratory, Berkeley, California 94720

D. P. Grote

Lawrence Livermore National Laboratory, Livermore, California 94551

(Received 17 September 1996; accepted 31 October 1996)

Current amplification of heavy-ion beams is an integral feature of the induction linac approach to heavy-ion fusion (HIF). In this paper we report on amplification experiments conducted on a single beam of the Multiple Beam Experiment (MBE-4), a heavy-ion (Cs^+) induction linac. Earlier MBE-4 experiments [H. Meuth *et al.*, Nucl. Instrum. Methods Phys. Res. A **278**, 153 (1989)] had demonstrated up-to- $9\times$ current amplification but had been accompanied by an up-to- $2\times$ increase of normalized transverse emittance. Experiments to pinpoint the causes of this emittance growth indicated various factors were responsible, including focusing aberrations and mismatch difficulties between the injector diode and the accelerator transport lattice, a localized quadrupole misalignment problem, and the interaction of transversely large beams with the nonlinear elements of the focusing lattice. Following ameliorative measures, new current amplification experiments, both with and without acceleration, showed that current amplifications of up to $3\times$ and line charge density increases of up to $\approx 2\times$ could be achieved without increasing the beam's normalized transverse emittance. Finally, both the transverse beam dynamics, and beam current and energy measurements were accurately modeled by numerical particle-in-cell simulations and longitudinal dynamics codes, respectively. © 1997 American Institute of Physics. [S1070-664X(97)01003-3]

I. INTRODUCTION

The Multiple Beam Experiment (MBE-4) at the Lawrence Berkeley National Laboratory (LBNL) was constructed to investigate beam dynamics issues relevant to the low-energy, electrostatically focused section of a heavy-ion induction linac driver for Inertial Fusion Energy (IFE). In the heavy-ion approach to IFE, the value of the transverse emittance is of critical importance in focusing the beam on the fusion target pellet. The requirement on the normalized emittance at the final focus as compared to that practically achievable from the injector determines a safety factor for any particular driver scenario. Although the normalized emittance will be conserved for a beam subject only to ideal optics and harmonic space-charge forces, one must anticipate some emittance growth from aberrations, nonlinear space-charge effects, alignment errors, transport mismatch, etc. While such phenomena are possible in all accelerators, heavy-ion IFE drivers are special in that they require a smooth and controlled temporal compression of the beam pulse from an $\approx 10\ \mu\text{s}$ duration at the injector to an $\approx 100\ \text{ns}$ duration at the accelerator exit. In general, this compression and the corresponding current amplification will also involve a smaller but not insignificant increase in the line charge density, λ . The magnitude of the increase, if any, of normalized transverse emittance during this compression is of crucial importance. Between the main accelerator and the final focus section, an additional $\sim 10\times$ “drift” (i.e., ballistic)

compression must also be applied to the beam pulse in order to bring the pulse duration down to the 10 ns necessary for fusion target ignition to occur.

In this paper we report on transverse emittance measurements in the MBE-4 accelerator, an experimental heavy-ion (Cs^+) induction linac. A major aim of the MBE-4 experimental program was to demonstrate the principle of controlled, stable current amplification in heavy-ion induction linacs. Because the Cs^+ ion beam velocities are nonrelativistic ($v_z \approx 0.0017c$ at 200 keV energy), it is possible to compress the temporal pulse width by differentially accelerating the tail of the beam with respect to the head, thus increasing the beam current. The differential acceleration leads to an energy “tilt” (at a given observation point in z) between the head and tail of the beam. Early experiments^{1,2} (circa 1985–1988) on MBE-4 resulted in up to $9\times$ current amplification from the injection value of 10 mA while the average beam energy was increased from 200 to 900 keV. Although these longitudinal dynamics studies successfully demonstrated current amplification, there was an accompanying increase in the normalized transverse emittance by as much as 75% to 100%. This was in contrast to the results of drifting beam experiments, where the normalized emittance appeared to remain constant. In an attempt to understand this unexpected and undesirable emittance growth, we shifted the focus of MBE-4 experiments during the 1989–1991 time period to transverse beam dynamics studies.

These new studies may be subdivided into two distinct areas. The first was essentially an investigation into the cause(s) of emittance growth during the 1985–1988 longitudinal compression studies with high currents. As explained

^{a)}Electronic mail: fawley@lbl.gov

^{b)}Present address: Laboratoire de l'Accélérateur Linéaire, Bâtiment 200, IN2P3-CNRS, Orsay 91405, France.

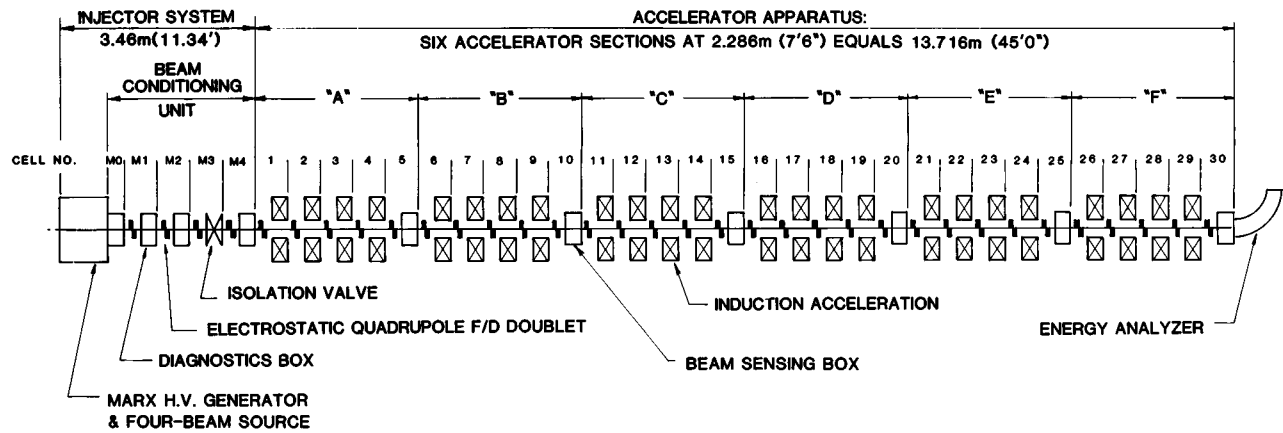


FIG. 1. Schematic of the MBE-4 accelerator.

in detail in Sec. III, focusing aberrations in the injector diode optics, mismatches in the matching section, and an apparent gross misalignment in accelerator section C (see Fig. 1) of the linac all played a role. Once these causes were eliminated or alleviated, we conducted a second set of compression studies with higher quality beams. We found (see Sec. IV) that transverse emittance growth should be acceptably small for reasonably moderate compression schedules, both with and without acceleration. As we discuss in our concluding section (Sec. V), these results scale well to an actual heavy-ion IFE driver, where the relative compression schedules will be far more gentle than those attempted in MBE-4. First, however, we describe in Sec. II important details concerning the actual accelerator system.

II. MBE-4 CHARACTERISTICS

A. General description

The MBE-4 injector produces four parallel beams of singly charged Cs^+ ions, which are then accelerated across a single diode gap to a nominal energy of 200 keV, the diode voltage being provided by a Marx generator with an inductively coupled pulse-flattening circuit. For reasons of simplicity, we performed the experiments discussed in this paper with only one source and beam of MBE-4. The relatively low, nonrelativistic perveances ($Q \equiv \lambda/4\pi\epsilon_0 V_b \leq 2 \times 10^{-3}$) and large separations between the individual beams imply that the interbeam forces are insignificant.

After crossing the diode gap, the beams enter a matching section that adjusts the beam envelope to provide a transverse phase-space distribution for transfer into the induction linac. From this point, the beams are transported through individual electrostatic, alternating gradient focusing channels while being accelerated across 24 common induction gaps. The linac contains six sections (denoted "A"–"F"), each comprising five lattice periods (LP), each of which has one long drift and one short drift space. In the first four periods of each section, the large drift space contains an acceleration gap. In the fifth period, this space is used for diagnostics and vacuum pumping. An energy analyzer and beam dump terminate section F. The accelerator is shown

schematically in Fig. 1; Ref. 3 contains additional information and figures regarding the overall MBE-4 accelerator.

B. Thermionic sources

The four Cs^+ beams thermionically originate from alumino-silicate layers coated on 19 mm radii molybdenum cups.⁴ The sources operate at a nominal temperature of 1000 °C and have extremely good pulse-to-pulse repeatability. From a series of pinhole pyrometry measurements made in 1990, the surface temperatures (and presumably the emission also) appeared uniform to within $\pm 5\%$. Typical source lifetimes are approximately two months before performance degrades due to a gradual mechanical delamination of the alumino-silicate layers. The extracted current from each source, 15.9 mA for a diode voltage of 180 kV, is space-charge limited for diode voltages in the 100–200 kV range and is in excellent agreement with predictions by the EGUN⁵ code. Our best normalized emittance measurements (see Sec. III A) downstream of the diode correspond to a calculated beam transverse energy of 0.2 eV, reasonably consistent with the measured surface temperature of 1000 °C ($=0.11$ eV).

C. Diode and matching section

The source cups are mounted on a Pierce-shaped, graphite anode plate that is electrically connected to an up-to-250-kV Marx generator. A timed crowbar switch sets the Marx pulse duration to 2.4 μs . The pulse rise time (0.25 μs) and shape are adjusted by adding correction pulsers to minimize voltage transients and to maintain a constant beam energy ($\Delta V/V \leq 0.2\%$).

The beams, focused along the anode–cathode gap of 133 mm, then freely pass through four holes in the grounded cathode plate into the MBE-4 matching section. There are no additional electrodes, grids, or other optics in the diode itself. The 1.83 m long matching section consists of four quadrupole doublets, each element being independently powered. Just beyond the first set of quadrupoles is a beam scraper plate with elliptical holes whose purpose is to reduce the beam current to 10 mA (this scraper effectively became superfluous when another, more limiting scraper was installed

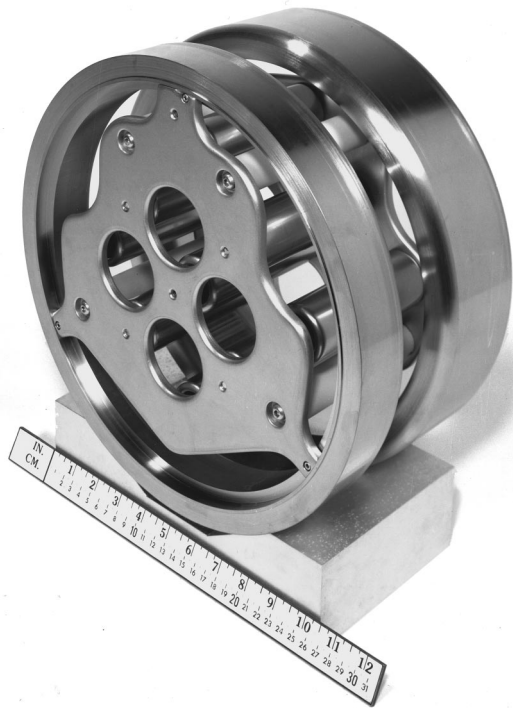


FIG. 2. Picture of an actual MBE-4 electrostatic quadrupole assembly.

in late 1989 just beyond the diode, as described in Sec. III A). Steering electrode arrays immediately followed by emittance diagnostics at the beginning and end of this section permit transverse beam alignment and phase space monitoring. Reference 7 gives additional details concerning the overall injector.

D. Induction linac cells and electrostatic focusing lattice

The actual linac consists of 24 accelerating gaps, each capable of producing up to 60 kV. The core assemblies include Ni-Fe cores recycled from the ASTRON accelerator⁶ and additional, newly purchased Si-Fe cores. The MBE-4 acceleration pulsers provide special ramped voltage waveforms to achieve the wanted differential acceleration along the beam current pulse. These waveforms also compensate for the “erosion” of the ends of the beam bunch caused by longitudinal space-charge forces, which required voltages from several pulsers to be superimposed at some gaps. A more complete discussion of the longitudinal dynamics and the determination of the acceleration “schedules” (i.e., different timings and amplitudes of the pulser waveforms) can be found in the Appendix and elsewhere.^{1,2,8,9}

Each quadrupole assembly (see Fig. 2) includes nine cylindrical electrode rods of 40.2 mm diameter and 107.4 mm length cantilevered from flat aperture plates, themselves surrounded by a conducting enclosure. The quadrupoles are arranged in a syncopated (i.e., FODO) lattice, where the “O” and “o” drift spaces are 178.3 and 64.1 mm long, respectively. The clear aperture between quadrupole rods is 54 mm. The focusing plane electrodes are held at ground potential while the defocusing plane electrodes are set typically at voltages of ~ -20 kV. This particular choice implies that the

beam accelerates as it enters a quadrupole and decelerates as it leaves. In addition to the dominant quadrupole focusing component, there is also a significant and intentional dodecapole component. Its rationale stems from earlier work,¹⁰ which indicated that a dodecapole of the right sign and magnitude could alleviate emittance growth arising from nonlinear image charge forces in off-center, space-charge dominated beams. The dodecapole magnitude is a function of the ratio of the quadrupole rod diameter to the clear aperture between the rods. A “magic” ratio of 1.1437 makes the dodecapole component disappear nearly exactly¹¹ in the two-dimensional (2-D) limit; earlier work¹² gave a somewhat less accurate result of 1.148. Reference 13 gives a detailed three-dimensional (3-D) multipole decomposition of the electrostatic fields (in the absence of beam space charge) within the MBE-4 quadrupole assembly.

Each unit cell (accelerating gap plus quadrupole focusing doublet) is 0.457 m long, resulting in an overall linac length of 13.7 m for the 30-period lattice. The quadrupole doublets in each accelerator section were initially (1985–1986) positioned to transverse accuracies of $75 \mu\text{m}$ (rms). Later measurements in June 1990 showed that, due to underlying concrete slab movement, individual sections had become misaligned by as much as $500 \mu\text{m}$. Following mechanical realignment, measurements conducted both before and after the set of experiments discussed in this paper indicated that the quadrupole transverse alignments remained accurate to $\approx 150 \mu\text{m}$ rms.

E. Diagnostics and data reduction

We used a standard Faraday cup with a 20 mm entrance radius to determine the time-dependent total current. Transverse emittance measurements were made using the familiar double-slit technique¹⁴ with a multishot scanning procedure to determine the time-dependent signal strength as a function of the transverse (x, x') phase space position, the charge being collected in a Faraday cup behind the downstream slit. Measurements were made in each transverse plane with typically 400 shots required for one complete emittance scan. We recorded the collected charge many (20–50) times during each shot with a ≈ 150 ns temporal resolution. In addition to transverse emittance, the collected data yield other time-resolved quantities of interest such as beam size, centroid position, and current profile integrated along the direction of the slits.

We defined the normalized “edge” emittance, $\pi\epsilon_n \equiv 4\pi\gamma\beta\epsilon_{\text{rms}}$, where

$$\epsilon_{\text{rms}}^2 \equiv (\langle x^2 \rangle - \langle x \rangle^2)(\langle x'^2 \rangle - \langle x' \rangle^2) - (\langle xx' \rangle - \langle x \rangle \langle x' \rangle)^2. \quad (1)$$

The factor of 4 is exact for a Kapchinskij–Vladimirskij (K–V)¹⁵ phase space distribution. During operation of the acceleration pulsers, we noticed that the Faraday cup signals were contaminated with electrical noise. In order to minimize such noise contributions (especially at the outer edge of the phase space plots where the beam signal is weak), we ignored data from phase space positions where the signal is below a cutoff level S_{min} . Typically, we set S_{min} to a level

that included $\approx 90\%$ or more of the total current. Hence, the averaging signified by the angle brackets of expression (1) is defined by

$$\langle f(t) \rangle \equiv \sum_{i,j} f(x_i, x'_j, t) S^*(x_i, x'_j, t) / \sum_{i,j} S^*(x_i, x'_j, t), \quad (2)$$

where $S^*(x_i, x'_j, t) \equiv \max[0, S(x_i, x'_j, t) - S_{\min}]$. While this treatment alleviates the noise problem, it can also artificially mask the presence of a low-intensity beam halo.

Two separate electrostatic analyzers determined the time-resolved energy distribution of the beam. The first analyzer is relatively large and can be positioned only at the end of the accelerator. Designed employing the analysis of Banford,¹⁶ it consists of two collimating 100 μm wide slits, 450 mm apart upstream of electrostatic deflecting plates and a wire detector. The deflecting plates are electrodes bent into coaxial cylindrical radii of 445 and 470 mm whose object and image planes are 152 mm in front and back of the plates. The practical energy resolution (determined by the wire diameter) is better than 0.2% while the time response is ≈ 10 ns. A typical energy scan required ~ 100 individual shots.

We also employed a second, much smaller energy analyzer that could fit in the diagnostic ports between accelerator sections. This compact analyzer includes two coaxial electrodes of 100 mm mean radius and 5 mm separation. Here 100 μm slits were placed in the object and image planes, themselves 48 mm in front and back of the electrodes. The analyzer is capable of measuring beam energies of up to 350 kV, limited by electrical breakdown in the dipole gap, with a resolution of 0.2%, determined by the slit width. The great majority of the energy analyzer data presented in Sec. IV originated from this second analyzer, for which absolute energy calibration was done through a series of drifting beam, time-of-flight measurements. Similar measurements were not done for the larger analyzer, which prevents an absolute comparison at LP30 between experiment and theory.

III. INVESTIGATION OF EMITTANCE GROWTH

A. Diode aberrations

As mentioned in the Introduction, early current amplification experiments with MBE-4 showed significant (1.75–2 \times) normalized transverse emittance growth. These experiments concentrated on demonstrating the simultaneous acceleration and longitudinal control of the four individual ion beams. The beam currents were relatively high, 10 mA, and we began to suspect that diode aberrations and beam mismatches in the transport line underlay some or all of the unwanted degradation. Detailed emittance and current profile measurements were made in early 1989 at the entrance into the matching section. As displayed in Fig. 3, the transverse phase-space profile had the characteristic “S” shape indicative of the presence of aberrations in the diode optics. Figure 3 also includes EGUN predictions for a zero-emittance beam. Approximately half of the measured normalized emittance, 0.08 mm mrad, was contributed by the “spiral arms” beyond the core “bar.” The diode’s overfocusing of the outer-

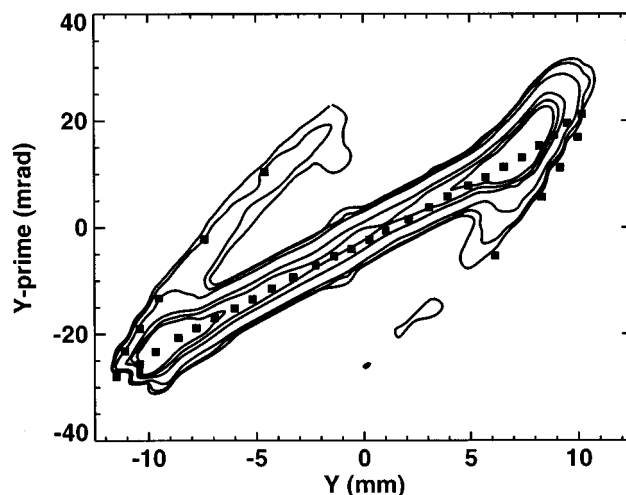


FIG. 3. Transverse phase space measurements of a 10 mA beam at the entrance to the matching zone showing the development of “spiral arms” due to anharmonic focusing forces in the injector. The contours levels enclose 97.5%, 95%, 90%, 70%, 50%, and 30% of the beam current. The solid boxes represent predictions from the EGUN code.

most rays of the beam led to enhanced current density at the beam edge and hollowing on axis (Fig. 4). Measurements farther downstream in the accelerator (Fig. 5) showed significant emittance oscillations in both transverse planes followed by damping. These we attribute to conversion of non-linear space-charge field energy to thermal energy via phase-mixed damping.^{17–19}

To obtain a higher quality beam, we placed a circular aperture ring (“scraper”) just beyond the cathode plate to reduce the beam current to ≈ 5 mA. Initially, we installed the aperture at the cathode plate but measurements suggested problems with secondary electron emission. To recapture those electrons, we biased the aperture to a positive 4.5 kV and recessed it 20 mm from the diode exit. After a series of experimental tests with different sized apertures, together with confirmatory EGUN calculations to optimize phase space and current density profiles, we settled upon an 11 mm diam. This particular choice passed 4.5 mA of the initial diode

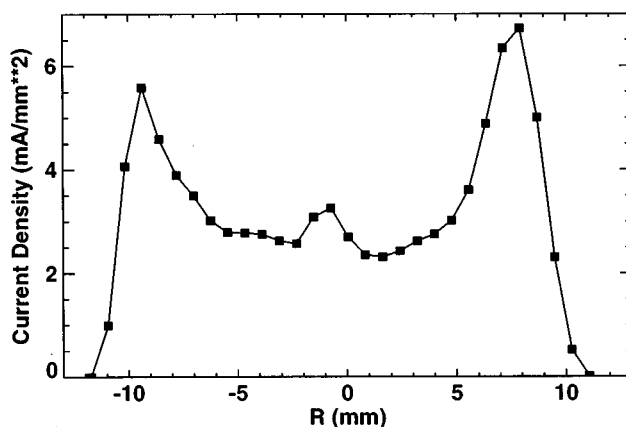


FIG. 4. Pinhole current density measurements made at the matching section entrance for the 10 mA beam of Fig. 3.

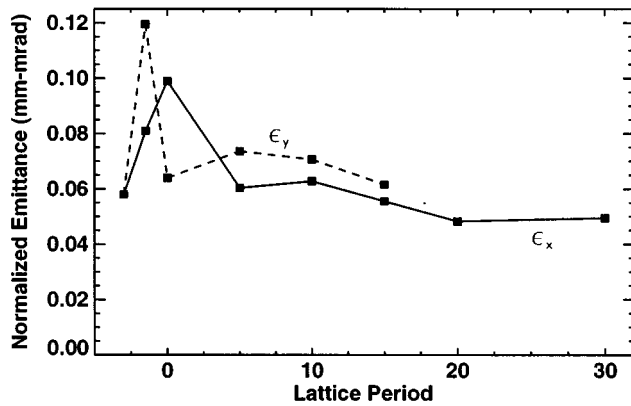


FIG. 5. Downstream normalized emittance measurements of the drifting 10 mA beam shown in Figs. 3 and 4. LP0 corresponds to the beginning of accelerator section A; the two negative positions lie within the matching section.

current. Beam current density measurements (Fig. 6) at the entrance into the matching section showed a much flatter profile and essentially no hollowing on axis. The measured transverse emittance (Fig. 7) decreased from 0.08 to 0.03 mm mrad, 1.4 times the theoretical minimum for a 1000 °C source temperature, thus resulting in a beam brightness $\approx 3\times$ greater than was true for the earlier, 10 mA beam. The aperture provides an additional benefit of reducing the maximum beam envelope from 14 to 10 mm downstream within the accelerator. Consequently, beam particles are less likely to experience strong nonlinear field components in the electrostatic focusing lattice.

B. Emittance growth in 4.5 mA drifting beam experiments

Following installation of the aperture ring, we examined the transport characteristics of a 4.5 mA beam merely drifting through the linac with the quadrupole focusing set to produce a zero-current phase advance σ_0 of 72° per full lattice period. Disturbingly, the emittance showed a general, but not monotonic, increase with longitudinal position (see

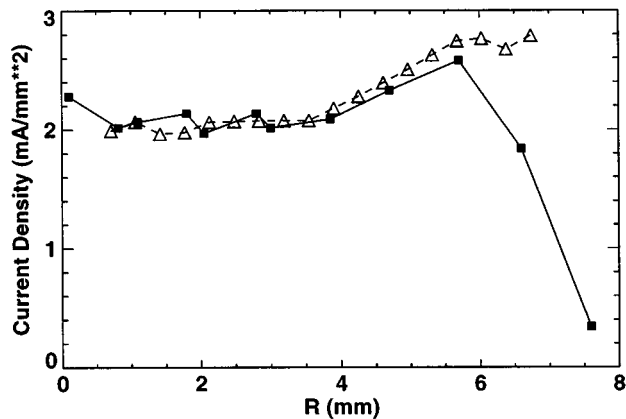


FIG. 6. Pinhole current density measurements (solid line, filled boxes) for the scraped, 4.5 mA beam together with corresponding EGUN code predictions (dashed line, open triangles).

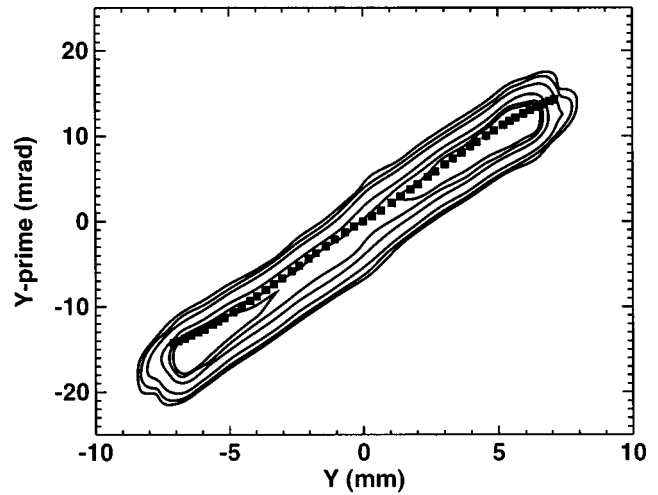


FIG. 7. Phase space measurements for the scraped 4.5 mA beam at the entrance into the matching section, together with corresponding EGUN code predictions. The contours levels enclose 97.5%, 95%, 90%, 70%, 50% and 30% of the beam current.

Fig. 8). Although this behavior is contrary to the earlier findings¹ with the drifting 10 mA beam (Fig. 5), the higher brightness of the lower current beam makes emittance growth far more obvious. The beam centroid also exhibited excursions of as much as 5 mm from the axis. Extensive efforts were then made to improve further the beam matching from the injector and beam steering at the injection point by minimizing positional and angular offsets. We then found that while the exact details of the emittance variation with z (of which Fig. 8 is a typical example) would depend upon items such as matching conditions or quadrupole voltages, emittance oscillations of up to $\pm 30\%$ would always appear from one diagnostic location to another. For a rigidly fixed initial condition, however, we established that the measured beam emittance at a given station was highly reproducible with less than 5% variation. We concluded that the different emittances measured on different occasions arose from changes in initial conditions, not from lack of measurement or machine repeatability.

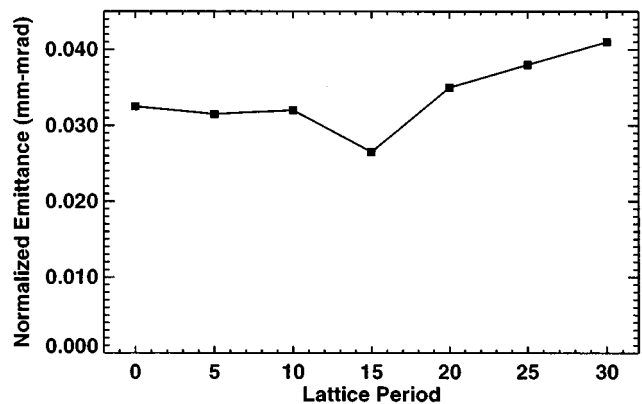


FIG. 8. Typical dependence of measured normalized emittance versus lattice period for a drifting 4.5 mA beam.

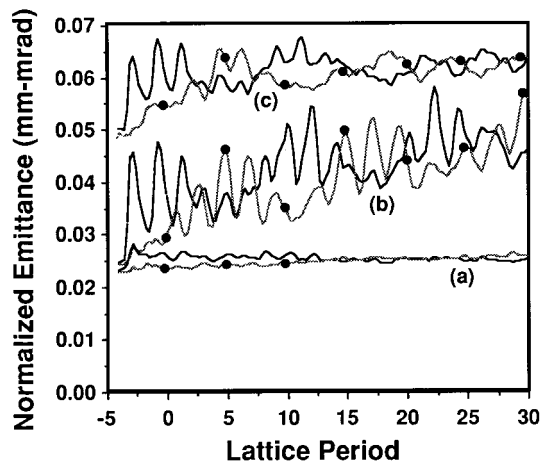


FIG. 9. SHIFT-XY simulation of the variation of horizontal and vertical (marked by the heavy dots) emittance for 4.5 mA beams injected into the MBE-4 focusing lattice with $\sigma_0 = 72^\circ$. In case (a), the beam was injected exactly on-axis, case (b) with an initial 3 mm offset in both x and y , and case (c) also offset 3 mm, but with the initial emittance doubled.

C. Numerical modeling results

In order to gain possible insights into these emittance variation phenomena, in parallel with the experimental effort we conducted numerical modeling studies of the MBE-4 system using a modified version of the electrostatic, 2-D particle-in-cell code SHIFT-XY.²⁰ The code follows a single, transverse beam slice beginning at injection just before the matching section between the diode and the linac. As input, we used measured values of the MBE-4 beam current, energy, rms emittance, and beam envelope parameters. The quadrupole focusing fields are treated as a thick lens with sharp edges in z . The code also includes the syncopated lattice structure. Via a capacity-matrix method, the transverse electric field solution includes the effects of image charges on the quadrupole rods (but not those on the flat aperture plates). The field solution also presumes periodic boundary conditions in both transverse planes. The LBNL version of the code includes gap acceleration and inclusion of the octupole and dodecapole components of the external focusing fields [but not fringe fields such as the “pseudo-octupole” component ($\propto r^3 \cos 2\theta$) arising from the second z derivative of the quadrupole field strength]. To minimize numerical noise, we employed ~ 64 K macroparticles on a uniform 128×128 or 256×256 Cartesian grid.

The results of the simulations can be summarized as follows: (i) in the absence of nonlinear fields, both off- and on-axis 4.5 mA beams propagate through the linac with no growth in the emittance, as expected; (ii) in the presence of nonlinear fields (such as those caused by image charges on the quadrupole rods or dodecapole focusing components), on-axis beams show essentially no emittance growth [Fig. 9(a)], whereas off-axis beams show continuous variations in emittance on top of a secular growth as the beam drifts through the linac [Fig. 9(b)]; (iii) details of the emittance variations depend greatly on the magnitude and direction of the beam displacement from the linac axis; (iv) offset beams with initially higher emittances suffer proportionally less

emittance growth and variations, although the change in $\Delta\epsilon^2$ remains more or less constant [Fig. 9(c)], as would be expected from conservation of energy arguments. The observed emittance growth is believed to result from the excitation of coherent beam modes, driven by the nonlinear forces and amplitude modulated by the coherent oscillation of the beam centroid. Previous simulations of the drift of a misaligned, space-charge dominated beam in a continuous electrostatic focusing lattice with nonlinear focusing components also showed emittance oscillations and growth.¹⁰

D. Variable σ_0 drift experiments

If the SHIFT-XY simulation results accurately predict drifting beam behavior in MBE-4, then the overall behavior results from specific initial conditions and transverse beam offsets. The observed z dependence of the emittance and centroid upon initial conditions such as seen in Fig. 8 is, in effect, an aliasing problem arising from the sparse experimental sampling rate (i.e., once per five lattice periods). Although we could not physically adjust the z spacing of the diagnostic locations, we used the following technique to scan the high-frequency behavior of the emittance and betatron oscillations at our existing diagnostic locations. By adjusting the zero-current phase advance per cell σ_0 (nominally 72°) via variation of the voltage of the focusing quadrupoles, we altered the total accumulated phase advance between injection and a fixed measurement location. This can be considered equivalent to changing the total number of periods traversed by a beam at given (nominal) unit-cell phase advance. The operating range in σ_0 was limited at the high end by beam envelope instability ($\sigma_0 \geq 85^\circ$) and at the low end by the beam envelope exceeding the useful quadrupole aperture ($\sigma_0 \leq 55^\circ$).

Using this technique, we quickly established that the betatron motion of the beam centroid had two primary constituents by LP25. The first, with an oscillation amplitude of ± 1.7 mm, appeared to originate near the entrance to the linac. This amplitude is consistent with random quadrupole offsets of $\approx 150 \mu\text{m}$, the alignment specification of MBE-4. The second and dominant constituent, which led to ± 4.5 mm amplitude oscillation, apparently originated at LP11 or LP12 in accelerator section C. We determined this location by measuring the phase variation of the beam centroid with σ_0 and making a comparison with numerical simulation. Examining Fig. 10, we see that both the amplitude of the measured emittance variations with σ_0 at LP25 and their oscillation frequency appear to be in good quantitative agreement with the SHIFT-XY results, as shown in Fig. 9. In both the experiment and simulation runs, the initial beam envelope parameters at LP0 were adjusted to produce a match for $\sigma_0 = 70^\circ$.

The kick at LP11/12 was first thought to originate from an electrical problem such as might develop from an unpowered quadrupole electrode or breakdown. However, after a month-long search failed to confirm this or the alternative explanation of a serious mechanical misalignment in section C, we decided to alleviate the problem by physically exchanging sections F and C and rotating the latter by 90° in order to proceed with our mainline experiments. After moving section C, it could not be determined if there was a

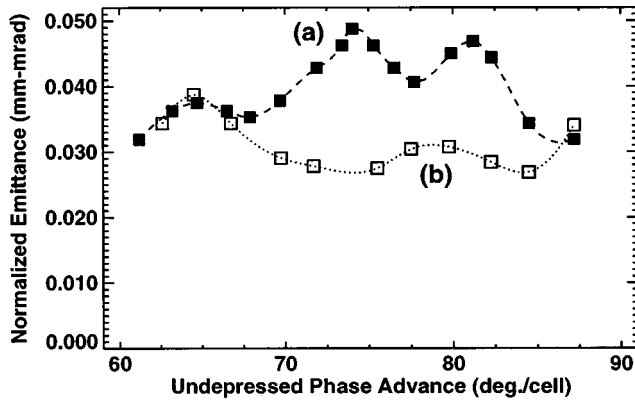


FIG. 10. Variation with σ_0 of the normalized emittance of a 4.5 mA beam measured at LP25. For comparison with Fig. 9, each 14° of phase advance is roughly equivalent to a difference of diagnostic location of five lattice periods. Curves (a) and (b) were taken before and after, respectively, the exchanges of section F for C. The lines through the points are from a simple spline fit.

mechanical problem related to vacuum pumpdown. At the time of this writing five years later, there is still no definitive understanding of the underlying problem with the original section C.

Following the exchange of linac sections C and F, we used dipole steerers to control offset errors at injection, and reduced the beam-centroid oscillation amplitude to ± 1.2 mm. The accompanying emittance variations with σ_0 at LP25 then decreased to less than $\approx 15\%$. Because beam offsets in any one transverse plane excite emittance oscillations in both planes, this residual emittance oscillation was probably due to uncorrected, small offsets in the vertical plane (which had one fewer dipole steerer than the horizontal plane). Returning the quadrupole focusing strength to $\sigma_0 = 72^\circ$, we then measured the z dependence of the emittance of an on-axis, drifting beam. As shown in Fig. 11 the emittance of a drifting 3.7 mA beam (a reduced current due to an aging source) remained constant in both planes and was much improved at LP30 as compared with the earlier measurement shown in Fig. 8.

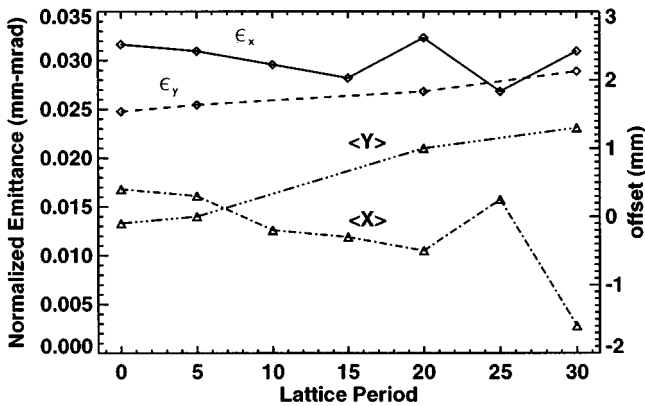


FIG. 11. Measured emittance and beam centroid positions versus z for a drifting, 4.5 mA beam following the exchange of linac section F for section C.

TABLE I. Emittance (ϵ) and beam radius (a) measurements for drift compression experiments.

I_{\max}/I_0	$\epsilon_{\text{rms}}^{\max}/\epsilon_{\text{rms}}^0$	a_{\max}/a_0	$\epsilon_{\mu}^{\max}/\epsilon_{\mu}^0$	LP _{max}
1:1	0.9–1.1	1.0–1.2	1.1–1.2	...
1.5:1	0.9–1.1	0.9–1.0	1.0	$\geq \text{LP20}$
3.7:1	1.3–1.6	1.6	1.0–1.2	LP25
7.4:1	≥ 2.8 –3.2	≥ 1.7 –2.0	≥ 2.1	LP20

IV. CURRENT AMPLIFICATION EXPERIMENTS

Having reduced the beam centroid motion and corresponding transverse emittance variations to an acceptably low level, we began a new series of current amplification studies. A particular concern was the dependence of transverse emittance growth, if any, upon the longitudinal compression rate. Previous 2-D simulation studies with the SHIFT-XY code suggested that compression can induce a minor radial profile (and nonlinear electrostatic energy) change, which can drive a small, but nonzero emittance increase, even in an ideal, AG focused transport channel. In this section, we first describe current amplification experiments on MBE-4 at essentially constant energy (i.e., drift compression that is relevant to modeling the final focus section of a HIF driver). We next discuss the results of some detailed 3-D particle-in-cell simulations of these experiments. In Sec. IV C we present current amplification experiments made with steady acceleration (which is relevant to the main linac section of a HIF driver).

A. Drift compression experiments

In the drift compression experiments, the amplitudes and timings of the pulsers in the first four accelerating gaps (section A) were adjusted empirically to put a nearly linear energy tilt on the beam. No further acceleration fields were applied downstream and the beam energy remained constant apart from the work done against the longitudinal space-charge field. The electrostatic quadrupole voltages were set for $\sigma_0 = 72^\circ$. No attempt was made to keep the beam envelope matched transversely as it compressed longitudinally. The space-charge depressed tune σ was in the range 7° – 10° .

Table I presents various measured quantities summarizing the results of the different drift compression schedules. A new quantity, the “microscopic” emittance ϵ_{μ} , was defined to be the phase space area (not necessarily contiguous) occupied by the most intense 80% fraction of the beam current. This quantity is readily extracted from the 2-D phase space map produced by the emittance scanner. Moreover, ϵ_{μ} is expected to be a more conserved quantity than ϵ_{rms} in cases such as a simple “S” or “Z” phase space distortion. In Table I, LP_{max} is the lattice period at which maximum compression was measured.

Our initial drift compression experiments employed a relatively large, 12% linear energy tilt that resulted in a nearly 5:1 current amplification by LP15 and 7.4:1 by LP20. Energy analyzer scans (see Fig. 12) show that the large velocity tilt at LP5 has been strongly reduced by LP20. Although detailed inspection of the energy scan at LP20 hints at some increase in longitudinal energy dispersion near the

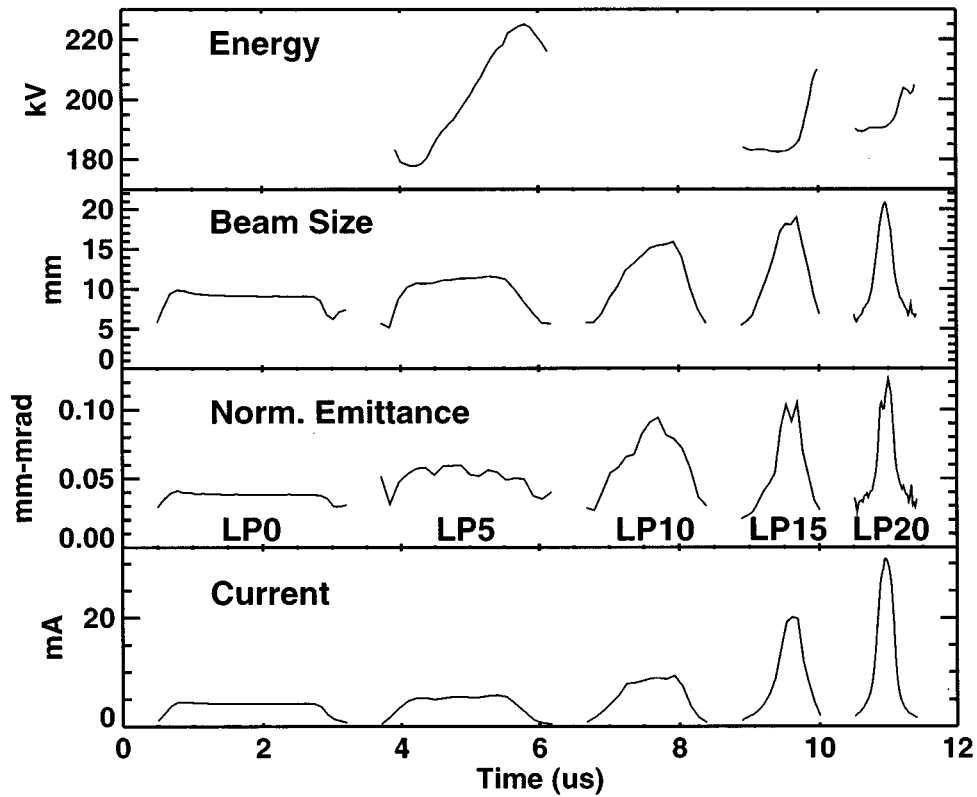


FIG. 12. Current, normalized emittance, beam size, and energy analyzer measurements of the 7.4:1 drift-compressed 4.5 mA beam. The data at different lattice points have been shifted in time relative to one another. The energy analyzer measurement at LP15, taken a couple of months before the data at LP5 and LP20, was plotted ≈ 10 kV downward to compensate for different injector conditions.

exact (temporal) center of the pulse, there is no obvious overtaking behavior (i.e., energy being a double-valued function of time). In the absence of strong overtaking, the coarseness in the energy analyzer step size (~ 0.25 kV), together with the large velocity tilt and the empirical sensitivity to small shot-to-shot timing and energy jitter, makes it nearly impossible to derive a quantitative measure of the instantaneous energy spread. One should note that the “Z” reversal present near the beam tail in the LP20 energy versus time plot in Fig. 12 is an unwanted feature. The desired result is a simultaneous reversal of the compression for all longitudinal portions of the current pulse [which would appear as a nearly vertical $E(t)$ dependence]. Achieving this result would require a very careful determination of the necessary acceleration schedules and equivalent pulser waveforms (for a given pulse shape) which was not done in this nor the accompanying drift compression experiments, with smaller energy tilt to be described shortly.

Although emittance scans of the 7.4:1 compression schedule showed that the beam centroid remained within 1 mm of the axis, the rms emittance tripled between LP0 and LP20. Moreover, the phase space data exhibited quite pronounced “butterfly” or “bowtie” shapes by LP15 and LP20, as shown in Fig. 13. The beam size increased from 9 mm at LP0 to at least 18 mm (and perhaps somewhat larger because the emittance scans were limited to ± 20 mm). This large beam size implies that the outer portions of the beam encountered relatively strong nonlinear focusing (primarily

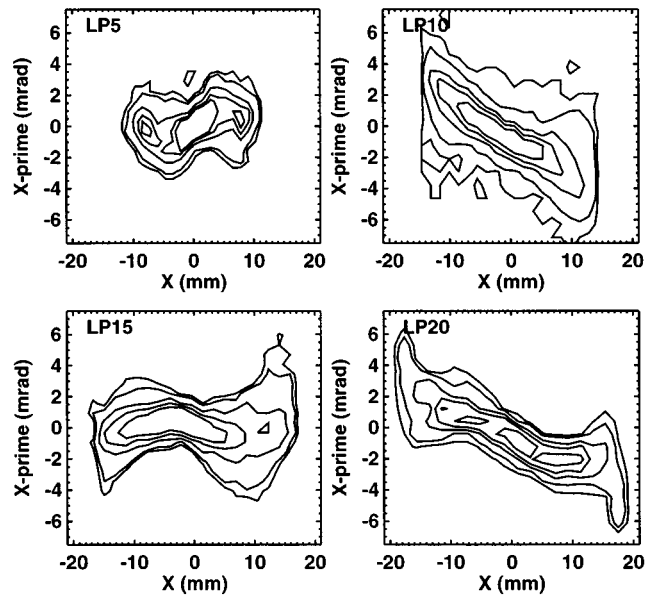


FIG. 13. Midpulse phase space density contours measured at different z locations for the central longitudinal slice of the 7.4:1 drift compression data. Via the experimental scanning procedure, the nominal linear correlation (i.e., tilt) of x' with x was removed in this and similar following figures. The contour levels correspond to enclosure of 95%, 90%, 70%, 50%, and 30% of the beam current.

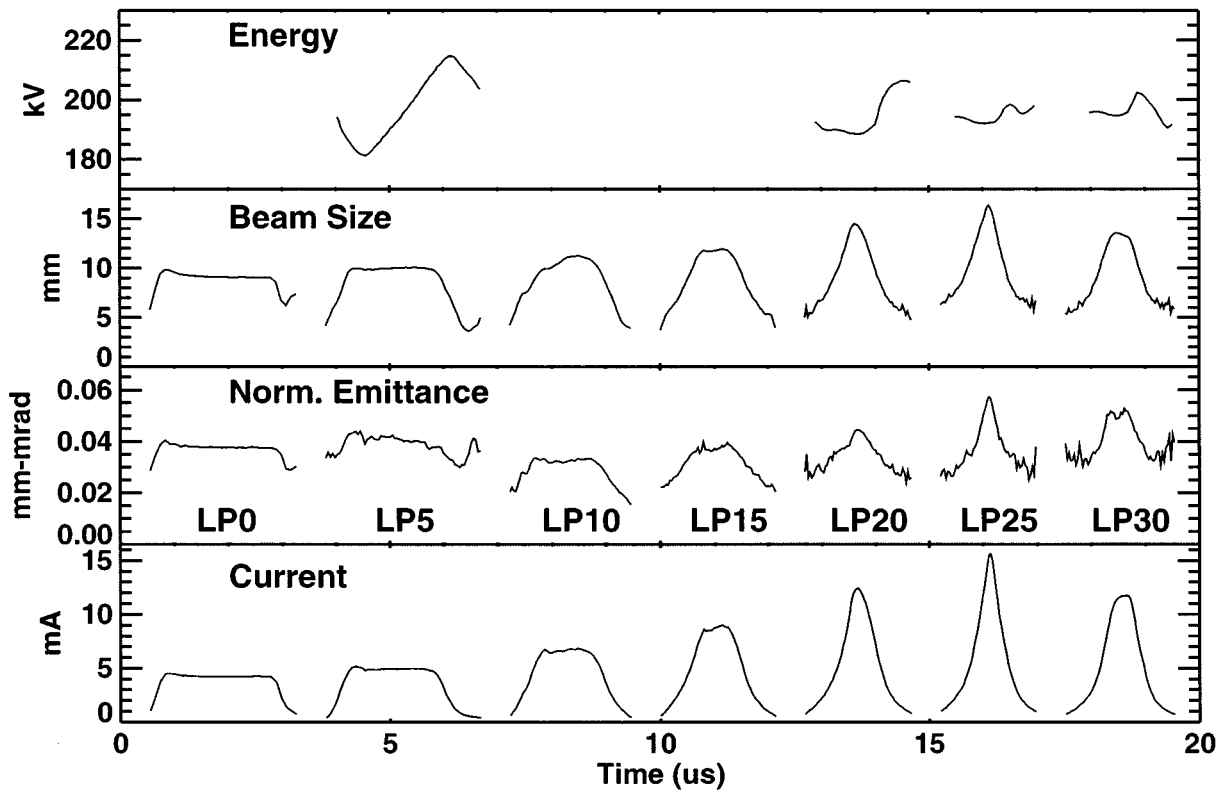


FIG. 14. Current, normalized emittance, beam size, and energy analyzer measurements of the 3.7:1 drift-compressed beam. As with Fig. 12, the data at different lattice point locations have been shifted in time relative to one another.

the dodecapole component) and image charge forces associated with the quadrupole rods at 27.4 mm. The butterfly shapes in phase space, the somewhat hollow radial profile in configuration space at LP20, and the 3-D simulation studies to be discussed in Sec. IV C all support this conclusion.

Since the 12% energy tilt appeared to be too extreme, we experimented with less vigorous tilts that would result in smaller compression factors and reduced maximum beam sizes. Our most complete drift compression dataset involved an initial head-to-tail energy tilt of 8.6% at LP5, which resulted in a maximum current amplification of 3.7:1 at LP25. Figure 14 shows current, emittance, beam size, and energy analyzer scans at the various z diagnostic locations. As before, there was no obvious longitudinal overtaking nor an obvious increase of instantaneous energy spread greater than the sampling step size of ~ 0.3 – 0.7 kV.

In Fig. 15 we plot $\epsilon(z)$ for various longitudinal slices of the beam pulse for this 3.7:1 compression schedule. The slices are labeled by their charge-weighted positions in the beam with the presumption that no longitudinal overtaking has occurred. Two observations are of note: (i) Slices with little compression ($I/I_0 \leq 2.7$) suffered little emittance growth and those in free expansion near the head and tail appear to have “cooled” with increasing z . (ii) Midpulse slices with significant emittance growth by LP25 showed little growth at earlier positions in z where the compression factor was ≤ 3.0 . Moreover, by LP30 their emittance returned close to the initial value at LP0. This and the fact that the microscopic emittance never increased significantly suggest that rather than an irreversible dilution of phase space (as would be true

if a halo formed in velocity space), the beam underwent a simple reversible shearing between LP15 and LP25. Inspection of phase space density contours (see Fig. 16) for the central longitudinal slice support this hypothesis. By contrast, the formation of “butterflies” or “bowties” in phase space (as was true in the 7.4:1 compression data) is most likely irreversible, this shape being indicative of particles

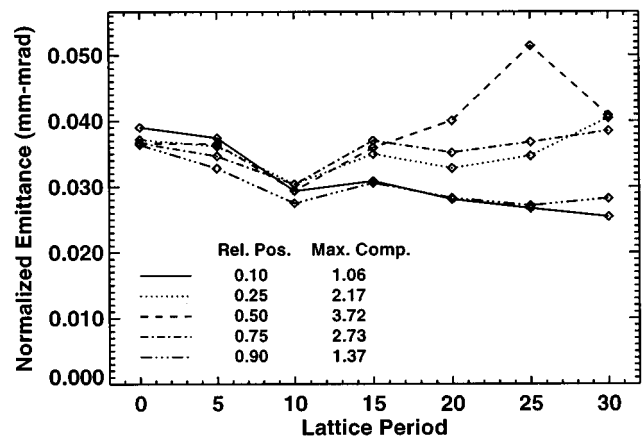


FIG. 15. Normalized emittance measurements for various longitudinal slices in the 3.7:1 drift compression data. The first number refers to the charge-weighted position in the beam (i.e., head=0, midpulse=0.5, tail=1) while the second refers to the maximum compression measured for a given longitudinal slice.

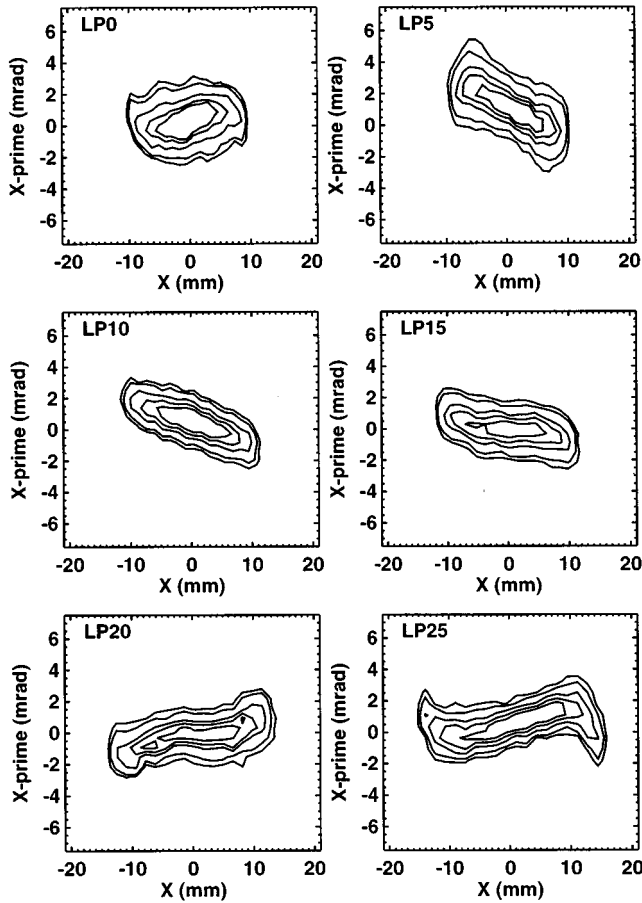


FIG. 16. Phase space density contours measured at different z locations for the central longitudinal slice of the 3.7:1 drift compression data. As in Fig. 13, the levels correspond to enclosure of 95%, 90%, 70%, 50%, and 30% of the beam current.

originally at larger radii overtaking those (transversely) at small radii.

Our mildest drift compression schedule resulted in 1.5:1 compression ratios by LP20. Although this schedule was sparsely diagnosed, there was no evidence of significant emittance growth or other anomalous behavior.

B. WARP3D code modeling of drift compression experiments

Following completion of the drift compression experiments, we were interested if numerical simulation could reproduce the results and pinpoint the underlying cause(s) of the emittance growth in the 7.4:1 compression schedule. In as much as the compression process inherently involves “3-D” phenomena, we used the WARP3D code²¹ for simulation studies (as opposed to using a 2-D code such as SHIFT-XY). WARP3D uses the PIC formulation together with a 3-D, Cartesian coordinate electrostatic field solver. A detailed explanation of the code physics and assumptions may be found in Ref. 22, which also contains a more extensive writeup of the MBE-4 simulation results summarized here.

For the WARP3D simulations we used beam parameters that were typical of the MBE-4 drift compression experi-

ments: $I_b = 5$ mA, $V = 180$ kV, $\epsilon_n = 0.026 \pi$ mm mrad, $a = 7.5$ mm, $a' = 21$ mrad, where a and a' are “edge” values measured at the center of a long drift section. The simulation adopted a “semi-Gaussian” (uniform in x - y space, Gaussian in velocity space) transverse phase space distribution. In order to load the beam in equilibrium and to prevent unphysical longitudinal and transverse distortion arising from the axial electric fields and energy variations associated with the $(0, -2V_q)$ asymmetric quadrupole focusing voltages (see Sec. II D), we injected the beam from a plane in the center of a long drift section. The number of macroparticles injected in each of the beam ends was varied in time to maintain a parabolic falloff in λ . No effort was made to adjust the beam envelope parameters at the ends; i.e., the same a , a' , and ϵ_n used in the center were also used in the lower line charge density ends. In order to determine the major contributions to the emittance growth, we did a systematic series of runs beginning with the “simplest” physical model (ideal, externally produced, sharp-edged quadrupole focusing without fringe fields, higher-order, nonlinear fields or image charges). We then added effects one by one until finally the most “complex” effects were included (actual, 3-D quadrupole rod geometry with full image charge and fringe fields, etc.) All of the simulation runs discussed here injected the beams in the same manner—with the envelope parameters chosen to provide equilibrium with ideal focusing fields.

The “simplest” simulation run, where the focusing was perfectly linear, resulted in less than 15% emittance growth for the most extreme initial velocity tilt. The square-shaped, conducting walls were placed 60 mm from the beam center, far enough away that image charge forces would be exceedingly weak. This small emittance increase was most likely a numerical artifact associated with the limited number of macroparticles ($\approx 3 \times 10^5$ employed). Adding perturbations such as an envelope mismatch led to emittance growth of 50% or less, which was nearly independent of the compression rate. This result disagrees with the experimental observations summarized in Table I, so we do not believe mismatch difficulties underlay the experimental emittance growth. Simulations begun with initially hollow beams and/or velocity ripples in v_z (as would be caused by accelerating gap pulser errors) showed similarly small emittance growth factors.

We then added an external dodecapole component to the focusing field whose amplitude at the position of the MBE-4 quadrupoles ($r = 27$ mm) was 3.5% of the quadrupole field, i.e. the value corresponding to the actual MBE-4 quadrupole array structure (see Sec. II D). For the most aggressively compressed beam, the maximum emittance increase was still only $\approx 50\%$ and the phase space “snapshots,” although distorted, did not resemble the “butterfly” shapes of Fig. 13.

A series of simulation runs with the conducting walls brought into $r = 27$ mm led to $\sim 3 \times$ emittance growth. Part of the increase stemmed from the lower values of the so-called “ g ” factor (see the Appendix) and resultant longitudinal electric fields that consequently increased the maximum compression obtained for a given initial velocity tilt. A more important influence was the image charges, which in this simulation lie much closer to the beam center (when

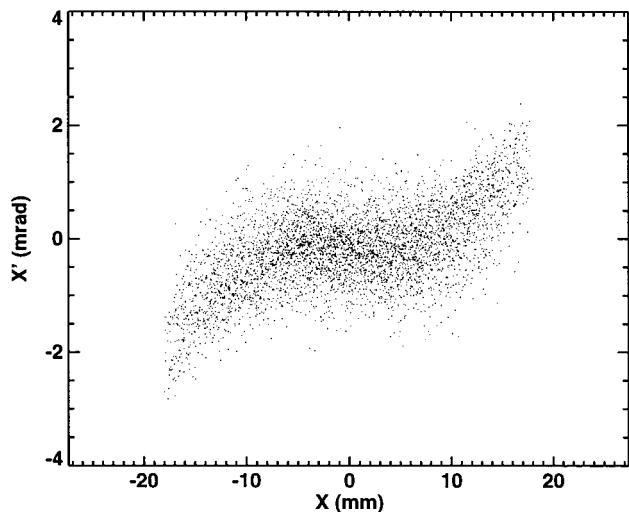


FIG. 17. Midpulse phase space distribution at maximum compression in a WARP3D simulation of a beam propagating in a square pipe 54 mm on a side. This particular simulation included image charges forces, but not those from the dodecapole focusing components.

averaged over a lattice period) than is true for the actual MBE-4 quadrupoles. The image charge fields, together with the larger beam size (≈ 19 mm) at maximum compression, produced sufficiently large nonlinear forces that a pronounced “Z” appeared in $x-x'$ phase space, together with large emittance growth at the pulse center (Fig. 17). Adding the dodecapole changed the details of the emittance evolution and phase space distribution but not the overall growth (in general, image charge forces produce “Z”-ing while higher-order nonlinear focusing terms such as the dodecapole produce “S”-ing in transverse phase space).

We then moved the conducting walls back to 60 mm and added correctly shaped quadrupole rods to the interior. Electrically, the rods were held at ground potential in the simulation (the focusing remained that of an externally applied, hard-edged, ideal quadrupole field). Thus, the rods’ only dynamical effects upon the beam particles arise from the induced image charge. As expected from the corresponding

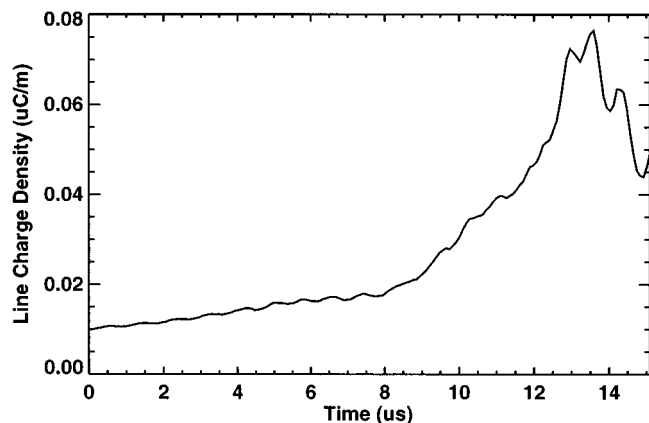


FIG. 18. WARP3D predictions for the midpulse, line charge density history of an aggressively compressed beam including the full interdigital quadrupole structure and field solution.

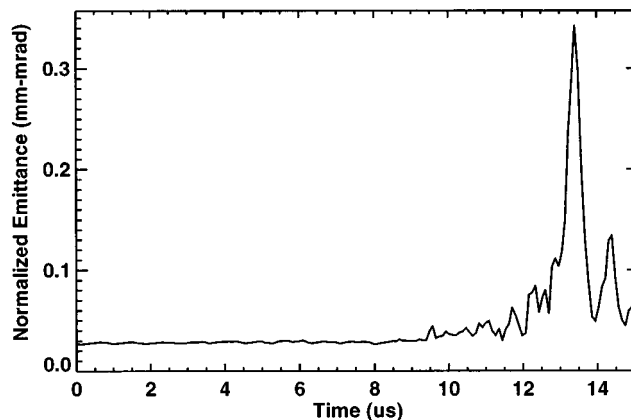


FIG. 19. Midpulse emittance history in the WARP3D simulation of the aggressively compressed beam.

increase in the average value of g and E_z , the maximum longitudinal compression dropped from 6.6 to $5.6\times$ and the net emittance growth to $\approx 2\times$. When an external dodecapole component was added, the net emittance gain decreased to less than 25%, confirming earlier 2-D simulation results¹⁰ that a dodecapole of the proper magnitude and sign could strongly reduce the emittance growth due to image charges.

Our final, most complete simulation set the internal quadrupole conductors to the actual focusing potential ($0, -2V_q$) together with the proper interdigital structure. The field solution then self-consistently produces the correct multipole fields, fringing field, image charges, and beam energy effects. This accuracy comes at a price, however: the required computation time increased by a factor of 6 [because of the use of an successive over-relaxation (SOR) field solver as compared with one based on fast Fourier transforms] to nearly two hours on a CRAY C-90. The results showed that the maximum compression increased to $7.6\times$ (Fig. 18) and the maximum beam radius increased to beyond 27 mm, the quadrupole aperture, although only a few macroparticles were lost in the simulation. The peak emittance growth was larger than $7\times$ (Fig. 19), although this growth persisted for only a short interval of transport distance. Most pleasingly, the phase space plots near midpulse in both $x-x'$ and $y-y'$ show the development of “bowties” (see Fig. 20). Diagnostic investigations involving correlation of configuration space positions with phase space positions indicate that the bowtie appearance arises from the strong dodecapole fields felt by macroparticles near the beam edge at maximum compression. Thus, it appears that the emittance growth cancellation effect between the image charge forces and the dodecapole component breaks down at large radius. Another emittance growth contribution may have been provided by the “pseudo-octupole” fringe field associated with the second z derivative of the quadrupole field produced by the finite length rods.

In recapitulation, then, our simulation results indicate that both image charge forces from a square conducting wall at ± 27 mm and/or dodecapole forces could cause relatively significant emittance growth ($\geq 3\times$) for beams whose maximum radii approached 19 mm. However, the resulting “Z”

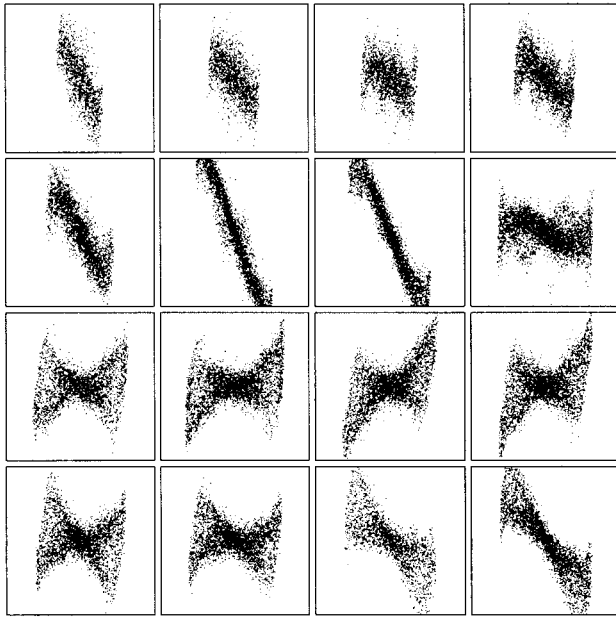


FIG. 20. The $x-x'$ phase space snapshots along the beam near maximum compression in the WARP3D simulation of Figs. 18 and 19. Each snapshot spans ± 27 mm in x and ± 5 mrad in x' .

or “S” shapes in phase space do not resemble the “butterflies” in the MBE-4 experiment. If the wall is replaced by conducting rods held at ground potential, the emittance growth is reduced to $\approx 2\times$ without dodecapole forces and to less than $1.25\times$ with these forces. Only when a full, self-consistent field solution is applied do we find good agreement between simulation and experiment, including both the bowtie/butterfly distortion in phase space and the overall increase in transverse emittance. In this last case, the beam envelope at maximum extent approaches the edges of the quadrupole rods and it is not surprising that significant beam quality degradation occurs.

C. Accelerated beam current amplification experiments

Following the drift compression experiments, we then began a series of current amplification experiments that include acceleration beyond LP5. We sought acceleration schedules that would produce a far less extreme current amplification than either the 9:1 schedules of Meuth *et al.*² or the most vigorous drift compression schedule discussed in the previous section. Our goal was to show that beams could

be simultaneously accelerated and compressed in MBE-4 without anomalous degradation of the normalized transverse emittance as long as the compression was suitably “adiabatic.”

In order to determine the proper schedule for a given compression, we used the following procedure. Powering each accelerator gap are several pulsed, whose timing and amplitude can be adjusted freely but whose waveforms are essentially fixed and measured at a resistive divider. A set of trial amplitudes and trigger timings, together with the measured beam current and energy profiles, are fed into a one-dimensional longitudinal dynamics code, SLIDE (see the Appendix). SLIDE then computes the predicted evolution of the time-dependent beam velocity and current as a function of z , including the longitudinal space-charge forces. After a series of iterations on the pulser amplitudes and timings, an “optimized” acceleration schedule is then dialed into MBE-4 itself. In general, we sought schedules that would lead to a steady and controlled compression without particle overtaking and balance the longitudinal space fields present at the beam head and tail regions that otherwise would cause expansion.

We obtained extensive experimental datasets on two particular acceleration schedules. The first, nicknamed “mild,” involved a general increase in beam energy from 180 kV at LP0 to 260 kV at LP15, together with an 8% head-to-tail energy tilt. The next two accelerator sections after LP15 provided an additional ~ 200 kV energy gain with no further energy tilt. The final acceleration section, “F,” added another 60 kV but, because of faulty and irreproducible behavior of its principal accelerating pulser, emittance data taken at LP30 was not usable.

The second schedule, nicknamed “gentle,” had a similar average acceleration rate through LP20, but the head-to-tail energy tilt (and thus compression rate) was increased to 12%. Moreover, the net voltage gain produced by the last two accelerator sections increased to 205 kV from 145 kV. Apart from the overall energy gain, the major difference between the two schedules is that the “gentle” schedule steadily compressed the pulse in time leading to a net current amplification factor of ≈ 3.2 by LP30 while the “mild” schedule produced a nearly constant pulse width beyond LP10.

In order to maintain a reasonably well-matched beam in the transverse plane during acceleration, we scaled the strengths of the quadrupole focusing voltages, V_q , proportional to the beam line-charge density, i.e. $V_q \propto \lambda \propto I/v$, where

TABLE II. Beam parameters versus z for the “mild” accelerated beam compression schedule.

z	I (mA)	τ_p (μ s)	$\langle V \rangle$ (kV)	ϵ_{rms} (mm mrad)	ϵ_n (mm mrad)	$2a_{rms}$ (mm)
LP0	4.53	2.30	179	5.4	0.035	9.1
LP5	4.61	2.30	179	5.6	0.039	9.0
LP10	4.96	2.15	246	4.3	0.036	8.8
LP15	5.41	2.00	262	4.5	0.038	10.1
LP20	5.62	1.86	346	3.9	0.038	10.8
LP25	5.42	2.01	430	3.7	0.040	10.0
LP30	5.96	2.02	493

TABLE III. Beam parameters versus z for the “gentle” accelerated beam compression schedule.

z	I (mA)	τ_p (μ s)	$\langle V \rangle$ (kV)	ϵ_{rms} (mm mrad)	ϵ_n (mm mrad)	$2a_{rms}$ (mm)
LP0	4.44	2.30	180	5.3	0.037	9.1
LP5	4.74	2.14	187	4.8	0.034	10.0
LP10	5.52	1.86	248	4.4	0.037	9.9
LP15	6.77	1.53	261	4.2	0.036	8.2
LP20	8.50	1.25	356	3.8	0.037	8.3
LP25	10.60	0.91	466	3.2	0.036	6.0
LP30	13.91	0.70	560

I and v are the beam current and longitudinal velocity, respectively. Ideally, to keep the matched beam radius constant, V_q should scale as $\lambda^{1/2}v$. The beam currents and velocities used in calculating the required voltages were determined from SLIDE results. Since electrical breakdown limits the maximum obtainable V_q on MBE-4, such scaling was not possible in the early Meuth *et al.* experiments,² where λ was increased by a factor of ~ 4.5 . The maximum beam radius for the “mild” and “gentle” acceleration schedules remained ≤ 11 mm, small enough that the effects of the external, nonlinear focusing forces should be unimportant.

Tables II and III summarize the beam measurements made with these two schedules. Encouragingly, the normalized emittance stayed constant to within $\approx 10\%$, even though the current more than doubled and the line charge density grew by a factor of ≈ 1.6 by LP25 for the “gentle” schedule. These results are much improved when compared with the earlier, more aggressive current amplification experiments of Meuth *et al.*,² which employed beams of initially higher currents but lower initial brightness.

We are also pleased by the excellent agreement between the SLIDE predictions for $I(t)$ and the Faraday cup measure-

ments at the diagnostic locations, as shown in Figs. 21 and 22. This agreement implies high accuracy in both the longitudinal field solution of SLIDE and the pulser waveform measurements. The only important discrepancy appears at LP25 for the “gentle” schedule where SLIDE predicts a “precursor” spike, whereas the Faraday cup measurements indicate that this spike has apparently disappeared between LP20 and LP25. For the “mild” schedule (Fig. 21), the precursor remains quite strong in both the experimental data and the SLIDE predictions at LP25 and LP30. This precursor steadily grows from LP0 onward and originates in the time-dependent voltage and impedance of the MBE-4 diode. In an actual heavy-ion IFE driver, it will be important to minimize or eliminate such phenomena.

SLIDE also predicts the time-dependent beam energy at each diagnostic location. For the “mild” schedule, we took data from the small energy analyzer at LP20 and the large energy analyzer at LP30. In Fig. 21 we plot $V(t)$ as predicted by SLIDE together with measurements at LP15, LP20, and LP30. We made the LP15 measurement by turning off the pulsers beyond LP15 and letting the beam drift to LP20, where the small energy analyzer was located. The change in beam energy due to longitudinal space-charge fields acting between LP15 and LP20 should be small (≤ 4 kV) over the main body of the pulse. Due to the lack of absolute energy

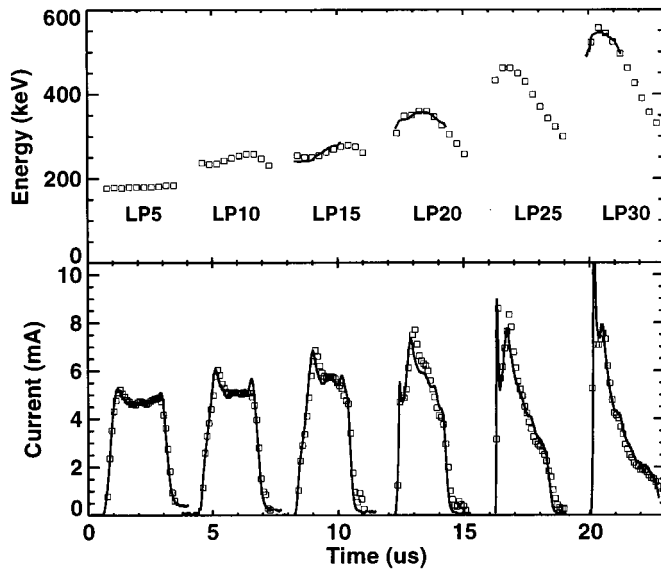


FIG. 21. Experimental measurements (solid lines) and SLIDE predictions (open boxes) for beam current and energy plotted versus time for a MBE-4 beam accelerated with the “mild” acceleration schedule. The curves have been shifted in time relative to one another.

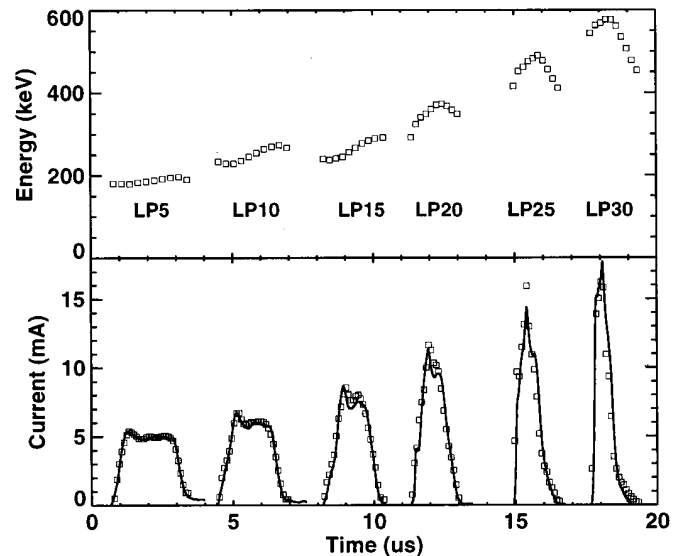


FIG. 22. The same as Fig. 21, but for the “gentle” acceleration schedule. No usable experimental energy measurements were available for this acceleration schedule.

calibration at LP30, we scaled the experimental energy data at this location to obtain a best fit in Fig. 21. At LP15 and LP20 the predictions and data are in good overall agreement, save for the first 0.5 μ s of the LP15 data being about 10 kV too high. Unfortunately, due to time constraints, energy analyzer measurements for the “gentle” schedule were made only at LP30 and suffered from the aforementioned problems with accelerating pulsers in section F. For the current, the predictions and data are again in good overall agreement (Fig. 22).

V. DISCUSSION AND CONCLUSIONS

As stressed in the Introduction, heavy-ion fusion driver accelerators are special in their need for smooth and controlled beam current amplification without an accompanying large degradation of beam quality in either the transverse or longitudinal planes. Consequently, we felt it important to understand and eliminate the causes of the transverse emittance growth found in the current amplification experiments performed during the first few years of MBE-4 operation. We believe that we succeeded in this endeavor, even though this meant using a multiple-beam accelerator in the “single-beam” mode.

To summarize our findings, it appears that the following elements were responsible for the emittance degradation in the early MBE-4 experiments.

- (1) Diode aberrations and mismatch difficulties that were pronounced for the large (i.e., 10 mA) currents used led to beam hollowing and consequent nonlinear space-charge forces downstream. As indicated in Sec. III A, we alleviated these problems by deploying a current “scraper” to reduce the transmitted current from the diode to 5 mA or less, and by working diligently both to obtain a good match to the accelerator focusing lattice and to minimize beam offsets.
- (2) An apparent misalignment problem in accelerator section C initiated additional transverse emittance growth via phase-mixed damping of the consequent transverse beam offset. We overcame this problem by exchanging sections C and F. Although earlier experiments showed that the emittance of a 10 mA, drifting beam remained approximately constant despite the above problems, this “constancy” was likely due to its injection emittance being sufficiently large to “hide” emittance growth that would have been far more obvious with much brighter beams. This assertion stems from both experimental and numerical simulation results (Secs. III B and III C; Ref. 23) that showed thermalized mismatch and displacement energy add in quadrature.
- (3) The relatively large envelope size of the 10 mA beam, which became even larger during strong longitudinal compression, resulted in a strong interaction with and emittance degradation due to the nonlinear dodecapole and fringe fields components associated with the MBE-4 quadrupole rod assembly.

These experiments reinforce the necessity of proper matching for emittance preservation of intense beams. This is certainly not a new idea and has received much theoretical

attention (e.g., see Refs. 17, 24). While in theory, a uniform beam in linear external focusing can be mismatched and displaced transversely without suffering emittance growth, space-charge dominated beams from imperfect injector optics transported in actual focusing lattices are virtually certain to encounter nonzero, nonlinear transverse force components that will thermalize mismatch and displacement energy into emittance.

Our new experimental results indicate that reasonable current amplification factors of $\approx 3:1$ or less for both drifting (Sec. IV A) and accelerated (Sec. IV C) beams are accompanied by little or no transverse normalized emittance growth for space-charge dominated beams with tune depressions $\sigma_0/\sigma \approx 10$. A key requirement appears to be keeping the compressed beam size sufficiently small that the effects of focusing nonlinearities (e.g., dodecapole components) will be minimal. One should also note the normalized compression rate, $(2L d\lambda/\lambda dz)/\sigma_0$, in these MBE-4 experiments ranged up to 0.05, which is an order of magnitude greater than that envisioned in most HIF driver scenarios. Thus, the apparent absence of emittance growth due to nonadiabatic, longitudinal compression is encouraging. However, the MBE-4 accelerator is also several orders of magnitude shorter than an actual driver in both real and normalized length, $\int \sigma_0 dz/2L$. Moreover, some driver scenarios may involve ballistic compression rates immediately before the final focus section that approach or even exceed normalized rates of 0.05.

Consequently, the operational shutdown of MBE-4 leaves us with guarded optimism that careful attention to proper matching and centering at injection, alignment of the transport lattice, and determination of the optimal acceleration and drift compression schedules in the main linac and final focus sections, respectively, will preserve adequate beam quality at the final target in a HIF driver. We are also left, however, with a desire for experiments at a scale far closer to real drivers so that this optimism can be replaced with a feeling closer to certainty.

ACKNOWLEDGMENTS

The authors are pleased to acknowledge the extensive hours put in by the MBE-4 technical staff to make all these experiments possible. We also wish to thank our past program managers in the Office of Basic Energy Sciences for providing a home and a commitment to the overall U.S. HIF program in the period 1986–1992.

This work was supported at LBNL and LLNL by the Director, Office of Energy Research, Offices of Basic Energy Science and Fusion Energy, U.S. Department of Energy, under Contracts No. DE-AC03-76SF00098 and No. W-7405-ENG-48.

APPENDIX: SLIDE NUMERICAL CODE

SLIDE is a one-dimensional particle-in-cell code that examines the longitudinal dynamics of nonrelativistic, space-charge dominated beams transported under the influence of longitudinal space-charge self-forces and external, real (imperfect) accelerating waveforms. SLIDE’s macroparticle formulation allows both particle overtaking and the resultant

longitudinal emittance degradation (which was a major limitation of its predecessor, the SLID code, whose physics was described in Ref. 9), and the injection of beams with an initial longitudinal velocity spread.

Basic assumptions in SLIDE include accelerating modules with infinitesimal gap widths and the electrostatic approximation for self-fields. The longitudinal space-charge field is calculated by the well-known long-wavelength approximation,

$$E_z \equiv \frac{-g}{4\pi\epsilon_0} \frac{d\lambda}{dz}, \quad \text{where } g \approx 0.5 + 2 \ln\left(\frac{b}{a_b}\right).$$

Here b is the effective conducting wall radius and a_b is the effective edge radius of the beam. From comparisons with energy and current profile measurements made on a drifting, 5 mA beam, we adopted a *constant* g factor of 2.8 for the SLIDE runs discussed in Sec. IV C. The uncertainty of this value is about ± 0.2 . For $b \approx 27$ mm, the clear aperture of the MBE-4 electrostatic quadrupoles, $g \equiv 2.8$ implies $a_b \approx 8.5$ mm, which agrees well with the measured values listed in Tables II and III.

We used the following procedure to determine a new acceleration “schedule:” First, we run a separate computer code, INDEX, to derive ideal accelerating fields by applying the so-called “current self-replicating” scheme.⁹ INDEX, however, neglects longitudinal space-charge forces. From this set of accelerating voltage waveforms, SLIDE then follows the evolution of the longitudinal particle distribution, now including the influence of longitudinal space-charge forces. If there are unwanted effects such as particle overtaking, INDEX can be run again seeking a less vigorous compression schedule. More general accelerating schedules as well as the effects of imperfections of the synthesized voltage waveforms on the longitudinal dynamics can also be analyzed by SLIDE. One convenient feature is that at any time step, the code can be put into “reverse” and run backward in time. This permits the user to back up and interactively change parameters, e.g. the peak voltage of a particular waveform.

SLIDE has been used extensively at LBNL to determine appropriate accelerating schedules as well as to analyze the longitudinal dynamics of ion beams for both actual experiments, such as those described in this paper, and for detailed design of the accelerating cell requirements of future HIF accelerators.

- ¹T. J. Fessenden, D. Keefe, C. Kim, H. Meuth, and A. Warwick, *Proceedings of the 1987 IEEE Particle Accelerator Conference*, Washington, DC, 1987, IEEE 87 CH2387-9 (Institute of Electrical and Electronics Engineers, New York, 1987), p. 898.
- ²H. Meuth, T. J. Fessenden, D. Keefe, and A. I. Warwick, *Nucl. Instrum. Methods Phys. Res. A* **278**, 153 (1989).
- ³R. T. Avery, C. S. Chavis, T. J. Fessenden, D. E. Gough, T. F. Henderson, D. Keefe, J. R. Meneghetti, C. D. Pike, D. L. Vanecek, and A. I. Warwick, *IEEE Trans. Nucl. Sci.* **NS-32**, 3187 (1985).
- ⁴A. I. Warwick, *IEEE Trans. Nucl. Sci.* **NS-32**, 1809 (1985).
- ⁵W. B. Herrmannsfeldt, in *Linear Accelerator and Beam Optics Codes*, AIP Conf. Proc. 177, edited by C. R. Eminhizer (American Institute of Physics, New York, 1988), p. 45.
- ⁶N. C. Christofilis, R. E. Hester, W. A. S. Lamb, D. D. Reagan, W. A. Sherwood, and R. E. Wright, *Rev. Sci. Instrum.* **35**, 886 (1964).
- ⁷A. I. Warwick, D. Vanecek, and O. Fredriksson, *IEEE Trans. Nucl. Sci.* **NS-32**, 3196 (1985).
- ⁸C. H. Kim, V. O. Brady, T. J. Fessenden, D. L. Judd, and L. J. Laslett, *IEEE Trans. Nucl. Sci.* **NS-32**, 3190 (1985).
- ⁹C. H. Kim and L. Smith, *Part. Accel.* **85**, 101 (1986).
- ¹⁰C. Celata, in Ref. 1, p. 996.
- ¹¹V. Brady and A. Faltens (private communication, 1988).
- ¹²I. E. Dayton, C. Shoemaker, and R. F. Mozler, *Rev. Sci. Instrum.* **25**, 485 (1954).
- ¹³M. Berz, W. M. Fawley, and K. Hahn, *Nucl. Instrum. Methods A* **307**, 1 (1991).
- ¹⁴M. J. Rhee and R. F. Schneider, *Part. Accel.* **20**, 133 (1986).
- ¹⁵I. M. Kapchinsky and V. V. Vladimirskij, *Proceedings of the 2nd International Conference on High Energy Accelerators and Instrumentation*, Geneva, 1959, edited by L. Kowarski (CERN Scientific Information Service, Geneva, 1959), p. 274.
- ¹⁶A. P. Banford, *The Transport of Charged Particle Beams* (E&F Spon, London, 1966), p. 84 ff.
- ¹⁷E. P. Lee, S. S. Yu, and W. A. Barletta, *Nucl. Fusion* **21**, 961 (1981).
- ¹⁸T. P. Wangler, K. R. Crandall, R. S. Mills, and M. Reiser, *IEEE Trans. Nucl. Sci.* **NS-32**, 2196 (1985).
- ¹⁹I. Hofmann and J. Struckmeier, *Part. Accel.* **21**, 69 (1987).
- ²⁰I. Haber, in *High Current, High Brightness, High Duty Factor Ion Injectors*, AIP Conf. Proc. 139, edited by G. H. Gillespie (American Institute of Physics, New York, 1986), p. 107.
- ²¹A. Friedman, D. P. Grote, D. A. Callahan, A. B. Langdon, and I. Haber, *Part. Accel.* **37–38**, 131 (1992).
- ²²D. P. Grote, Ph.D. thesis, University of California, Davis, 1994. Reprinted as National Technical Service Document No. DE96000393 (*Three Dimensional Simulations of Space Charge Dominated Heavy Ion Beams with Applications to Inertial Fusion Energy*, Lawrence Livermore National Laboratory, Livermore, CA, UCRL-LR-119363). Copies may be ordered from the National Technical Information Service, Springfield, VA 22161.
- ²³T. Garvey, S. Eylon, T. J. Fessenden, and E. Henestroza, *Part. Accel.* **37–38**, 241 (1992).
- ²⁴M. Reiser, *J. Appl. Phys.* **70**, 1919 (1991).